Atmos. Chem. Phys., 21, 9839–9857, 2021
https://doi.org/10.5194/acp-21-9839-2021

Atmospheric Chemistry and Physics
Open Access
EGU

Contributions of equatorial waves and small-scale convective gravity waves to the 2019/20 quasi-biennial oscillation (QBO) disruption

Min-Jee Kang and Hye-Yeong Chun

Department of Atmospheric Sciences, Yonsei University, Seoul, South Korea

Correspondence: Hye-Yeong Chun (chunhy@yonsei.ac.kr)

Received: 29 January 2021 – Discussion started: 1 March 2021
Revised: 6 May 2021 – Accepted: 2 June 2021 – Published: 1 July 2021

Abstract. In January 2020, unexpected easterly winds developed in the downward-propagating westerly quasi-biennial oscillation (QBO) phase. This event corresponds to the second QBO disruption in history, and it occurred 4 years after the first disruption of 2015/16. According to several previous studies, strong midlatitude Rossby waves propagating from the Southern Hemisphere (SH) during the SH winter likely initiated the disruption; nevertheless, the wave forcing that finally led to the disruption has not been investigated. In this study, we examine the role of equatorial waves and small-scale convective gravity waves (CGWs) in the 2019/20 QBO disruption using Modern-Era Retrospective Analysis for Research and Applications version 2 (MERRA-2) global reanalysis data.

In June–September 2019, unusually strong Rossby wave forcing originating from the SH decelerated the westerly QBO at 0–5° N at ∼ 50 hPa. In October–November 2019, vertically (horizontally) propagating Rossby waves and mixed Rossby–gravity (MRG) waves began to increase (decrease). From December 2019, the contribution of the MRG wave forcing to the zonal wind deceleration was the largest, followed by the Rossby wave forcing originating from the Northern Hemisphere and the equatorial troposphere. In January 2020, CGWs provided 11 % of the total negative wave forcing at ∼ 43 hPa. Inertia–gravity (IG) waves exhibited a moderate contribution to the negative forcing throughout. Although the zonal mean precipitation was not significantly larger than the climatology, convectively coupled equatorial wave activities were increased during the 2019/20 disruption. As in the 2015/16 QBO disruption, the increased barotropic instability at the QBO edges generated more MRG waves at 70–90 hPa, and westerly anomalies in the upper troposphere allowed more westward IG waves and CGWs to propagate to the stratosphere. Combining the 2015/16 and 2019/20 disruption cases, Rossby waves and MRG waves can be considered the key factors inducing QBO disruption.

1 Introduction

The quasi-biennial oscillation (QBO) was first recorded through radiosonde wind observations in 1953 (Ebdon, 1960; Reed et al., 1961; Naujokat, 1986). Since then, a QBO phase transition has been made regularly by the descent of the opposite QBO phase with periods of 20–35 months. However, in February 2016, easterly forcing in the middle of the westerly winds disrupted the downward-propagating westerly QBO for the first time (Osprey et al., 2016), which is referred to as the 2015/16 QBO disruption. Because the QBO phase is highly correlated with extratropical and tropospheric phenomena, the impact of the disarrangement of the westerly QBO phase by the sudden development of the easterly winds was not limited to the equatorial stratosphere (Tweedy et al., 2017). The 2015/16 QBO disruption was primarily caused by equatorially propagating Rossby wave forcing. The large magnitude of the Rossby wave flux in the Northern Hemisphere (NH) midlatitudes (Osprey et al., 2016; Coy et al., 2017; Hirota et al., 2018) and its increased amount of equatorward propagation by the strong subtropical westerlies in the lower stratosphere (Barton and McCormack, 2017) likely induced the QBO disruption. However, the enhanced equatorial wave forcing also contributed to the 2015/16 QBO disruption, which was first mentioned by Lin et al. (2019) and analyzed in detail by Kang et al. (2020; KCG20 hereafter), who investigated each type of equatorial wave and small-

scale convective gravity waves (CGWs) during the 2015/16 QBO disruption.

According to KCG20, inertia–gravity (IG) waves and mixed Rossby–gravity (MRG) waves at the altitude range of 40–50 hPa in October–November 2015 preconditioned the zonal wind to be susceptible to the extratropical Rossby waves. In the later stage, Rossby waves originating from the NH midlatitudes and the equatorial troposphere to the equatorial stratosphere decelerated the QBO jet core due to their considerably large magnitude compared to the climatology. In the final stage of the disruption, the small-scale CGW forcing contributed to strengthening of the negative vertical wind shear by 20 % of all negative wave forcing. In October 2015–February 2016, stratospheric equatorial waves were unusually strong on account of the exceptionally strong tropospheric convective activity. Moreover, the magnitude of westward-propagating IG waves and CGWs was larger than that of the eastward waves, probably due to the positive zonal wind anomalies at 70–200 hPa. The strong MRG wave forcing was most likely generated from the increased barotropic instability at the QBO edges in the lower stratosphere.

Surprisingly, in January 2020, the westerly QBO phase was once again disrupted by the easterly winds at 43 hPa. This occurrence suggests that the 2015/16 QBO disruption is not a single event and that QBO disruption may occur more frequently in the future. Actually, the possibility of a second QBO disruption was already raised by Raphaldini et al. (2020), who demonstrated that the wind system related to an asymmetric zonal Rossby mode underwent a critical transition (Dakos et al., 2012) around 2016. Anstey et al. (2020) suggested that large horizontal momentum flux in the Southern Hemisphere (SH) propagating into the tropics in June–September 2019 served as the most significant cause of the 2019/20 QBO disruption. The wave flux was not exceptionally strong after that period; however, the persistent wave forcing finally disrupted the westerly winds at 43 hPa in January 2020. In the austral winter of 2019, Rossby wave activity in the stratosphere was anomalously and sufficiently strong to induce a minor sudden stratospheric warming (SSW) (Eswaraiah et al., 2020; Shen et al., 2020). Therefore, it is likely that the strong extratropical Rossby waves during the SH winter initiated the 2019/20 QBO disruption. Nevertheless, a dominant wave forcing from October 2019 to January 2020, which finally reversed the zonal wind sign, has not been examined yet, and the possible contributions from the equatorially trapped waves remain to be investigated.

In this study, we provide a comprehensive overview of the 2019/20 QBO disruption by examining all the equatorial waves (Kelvin, Rossby, MRG, and IG waves) and small-scale CGWs as in KCG20. To this end, we separate each equatorial wave mode (Kim and Chun, 2015) and evaluate small-scale CGW forcing by using an offline CGW parameterization with Modern-Era Retrospective Analysis for Research and Applications version 2 (MERRA-2) reanalysis data (Gelaro et al., 2017). It should be noted that the same analysis tool and figure style as those in KCG20 are adopted to compare the 2015/16 and 2019/20 QBO disruptions. Section 2 describes the adopted reanalysis data and methods. Section 3 discusses the morphology of the equatorial waves and zonal wind (Sect. 3.1) as well as the quantitative estimation of each equatorial wave forcing and small-scale CGW forcing (Sect. 3.2) during the 2019/20 QBO disruption. In addition, the characteristics (including sources) of Rossby, MRG, IG, and small-scale CGWs are evaluated in Sects. 3.3–3.6, along with a summary of the key differences between 2015/16 and 2019/20 QBO disruptions in Sect. 3.7. Section 4 provides the concluding remarks.

2 Data and methods

2.1 Reanalysis data

We use 3-hourly output of MERRA-2 reanalysis data provided on a lat 0.5° × long 0.625° grid at a native model level from January 1980 to July 2020 (GMAO, 2015) with the same variables as in KCG20.

The QBO was originally in the westerly phase when the 2019/20 QBO disruption happened. In order to examine the difference between the climatological westerly QBO and the 2019/20 QBO disruption, we select the years with a westerly QBO when the monthly mean zonal wind is more westerly than the monthly climatology by more than +0.5 SD at both 30 and 50 hPa for at least 4 months during the 6 months from April to September: 1980/81, 1985/86, 1990/91, 1993/94, 1995/96, 1997/98, 1999/2000, 2002/03, 2004/05, 2006/07, and 2011/12. This method ensures that the average of the 11 years, referred to in this study as the climatology, exhibits a downward QBO phase progression similar to that in 2019/20 (see Fig. 3).

2.2 Methods

The temporal evolution of the zonal-mean zonal wind is investigated using the transformed Eulerian mean (TEM) zonal momentum equation (Andrews et al., 1987):

$$\frac{\partial \overline{u}}{\partial t} = \left(f - \frac{1}{a\cos\phi}\frac{\partial}{\partial \phi}\left(\overline{u}\cos\phi\right)\right)\overline{v}^* - \overline{w}^*\frac{\partial \overline{u}}{\partial z} + \frac{1}{\rho_0 a\cos\phi}\nabla\cdot F + \overline{X}, \quad (1)$$

where u, v, and w are zonal wind, meridional wind, and vertical velocity, respectively, and the overbar denotes the zonal average. Here, z is the log-pressure height, which is defined as $-H\ln(p/p_s)$, where H, p, and p_s are the scale height, pressure, and surface pressure, respectively. a is the radius of the Earth, ρ_0 is the background air density, and ϕ is the latitude. $\overline{v}^*$ and $\overline{w}^*$ are defined by $\overline{v}^* = \overline{v} - \rho_0^{-1}(\rho_0\overline{v'\theta'}/\overline{\theta}_z)_z$ and $\overline{w}^* = \overline{w} + (a\cos\phi)^{-1}(\cos\phi\overline{v'\theta'}/\overline{\theta}_z)_\phi$, which represent the residual meridional and vertical velocities, respectively.

The term $\frac{1}{\rho_0 a\cos\phi}\nabla\cdot F$ represents the Eliassen–Palm flux (EPF) divergence (EPFD):

$$\frac{1}{\rho_0 a\cos\phi}\nabla\cdot F = \frac{1}{\rho_0 a\cos\phi} \cdot\left[\frac{1}{a\cos\phi}\frac{\partial}{\partial\phi}\left(F^{\phi}\cos\phi\right)+\frac{\partial F^{z}}{\partial z}\right], \quad (2)$$

where F^{ϕ} $[F^{\phi}=\rho_0 a\cos\phi(-\overline{u'v'}+\overline{u}_z\overline{v'\theta'}/\overline{\theta}_z)]$ and F^{z} $[F^{z}=\rho_0 a\cos\phi((f-1/(a\cos\phi)\partial/\partial\phi(\overline{u}\cos\phi))\overline{v'\theta'}/\overline{\theta}_z-\overline{u'w'})]$ denote the meridional and vertical components of the EPF, respectively. The first and second terms of the F^z are referred to as F^{z1} and F^{z2}, respectively. The $\overline{X}$ term denotes the residual term, which includes the parameterized GWD.

In the equatorial region, the EPFD is calculated for each equatorial wave mode (Kelvin, Rossby, MRG, and IG waves). The separation method is the same as that used in KCG20, following the method of Kim and Chun (2015). That is, in the wavenumber–frequency ($k-\omega$) domain obtained from a two-dimensional (longitude and time) Fourier transform with a 90 d window, spectral components with $|F^{z1}|<|F^{z2}|$ in the range of $0<k\le 20$ and $\omega<0.75\,\mathrm{cycle\,d^{-1}}$ (cpd) in the symmetric spectrum are considered Kelvin waves, and the spectral components with $F^{z1}\times F^{z2}<0$ in the range of $|k|\le 20$ and $0.1\le\omega\le 0.5$ cpd in the antisymmetric spectrum are considered MRG waves. Among the spectral components not classified as either of these wave types, those in the ranges of $|k|\le 20$ and $\omega\le 0.4$ are defined as Rossby waves, with the remainder defined as IG waves. In the troposphere (below 100 hPa), IG waves are defined as (i) $|k|>20$ or (ii) $|k|\le 20$ and $\omega>0.4$ cpd. The source level of the IG waves in the troposphere is assumed to be 140 hPa (see KCG20). EPFD for each equatorial wave mode is calculated using Parseval's theorem.

To obtain small-scale CGW forcing constituting $\overline{X}$, an offline CGW parameterization is performed as in KCG20. First, the phase-speed spectrum of the GW momentum flux generated from the diabatic forcing at the source level (cloud top) is calculated. Second, the GW momentum flux and drag are calculated based on Lindzen's saturation scheme (Lindzen, 1981) based on columnar propagation. It should be noted that, in order to constrain the magnitude of the CGW momentum flux obtained from an offline parameterization to prevent overestimation or underestimation of the CGW forcing, we use GWs observed from super-pressure balloons in the tropical region (Jewtoukoff et al., 2013) (see Kang et al., 2017), as in KCG20. The small-scale CGWs considered in this study have horizontal wavelengths smaller than 100–200 km. The details of the parameterization scheme of the CGWs can be found in KCG20.

As a key source of equatorial waves, convective activity is investigated using the precipitation data provided by MERRA-2. In addition, barotropic instability at the QBO edges is investigated as a potential source of MRG waves (Garcia and Richter, 2019; KCG20):

$$\overline{q}_{\phi}=2\Omega\cos\phi-\left[\frac{(\overline{u}\cos\phi)_{\phi}}{a\cos\phi}\right]_{\phi}-\frac{a}{\rho_0}\left(\frac{\rho_0 f^2}{N^2}\overline{u}_z\right)_z. \quad (3)$$

The negative regions of $\overline{q}_{\phi}$ indicate baroclinic and/or barotropic instability.

3 Results

3.1 Morphology of the zonal wind and each type of wave

Figure 1 shows the latitude–height cross section of the zonal-mean zonal wind from July 2019 to January 2020 with the corresponding monthly climatology (Fig. 1a) and the vertical profile of the zonal-mean zonal wind averaged for 5° N–5° S from July 2019 to January 2020 overlaid with the climatology (Fig. 1b). As early as July 2019, the northern side of the WQBO jet starts to be deformed. In September 2019, the westerly jet becomes weak at the altitude range of 40–50 hPa by more than 1σ (Fig. 1b). Thereafter, the westerly wind at 43 hPa begins to decelerate, changing to easterly in January 2020. The 2019/20 QBO disruption period shows a weaker westerly wind at altitudes near 30 hPa and a shallower WQBO jet compared to that in the 2015/16 QBO disruption period (Fig. 1 of KCG20). At 100–150 hPa, positive wind shear anomalies compared to the climatology are observed in July–December 2019, while westerly anomalies are observed in January 2020.

Figure 2 shows the EPF and EPFD for each equatorial wave as well as the CGWs in a latitude–height cross section in January 2020. The EPF and EPFD are each multiplied by a factor of 2, except for the Rossby waves, to suitably represent the morphology of each wave. The P-CGWs (Fig. 2a) exhibit a positive (negative) forcing at 60–80 hPa (20–30 hPa and $\sim$ 50 hPa), which is the strongest at 20 hPa over 5° N–5° S. Close to the Equator, the negative CGW forcing is stronger than the climatology by more than 1σ at 50–60 hPa.

In the lower stratosphere (60–100 hPa), Kelvin waves exert positive forcing on the QBO jet, thereby maintaining the westerly jet below the easterly wind development (Fig. 2b). However, the Kelvin wave forcing at 20–30 hPa is considerably smaller than that in February 2016 (Fig. 2b of KCG20); this is because the upper jet is very weak. The Kelvin waves propagating from the troposphere are larger than the climatology (Fig. S1 in the Supplement), though the increase is less than that in January and February 2016. The lesser increase is probably due to the absence of the strong El Niño during 2019/20, unlike in the 2015/16 disruption period. The same EPF and EPFD as in Fig. 2 but from July 2019 to February 2020 are shown in Fig. S3 in the Supplement.

MRG waves provide a strong negative forcing to the zonal wind at 25–100 hPa, concentrated at the Equator (Fig. 2c). The negative MRG wave forcing at 40–50 hPa, which is crit-

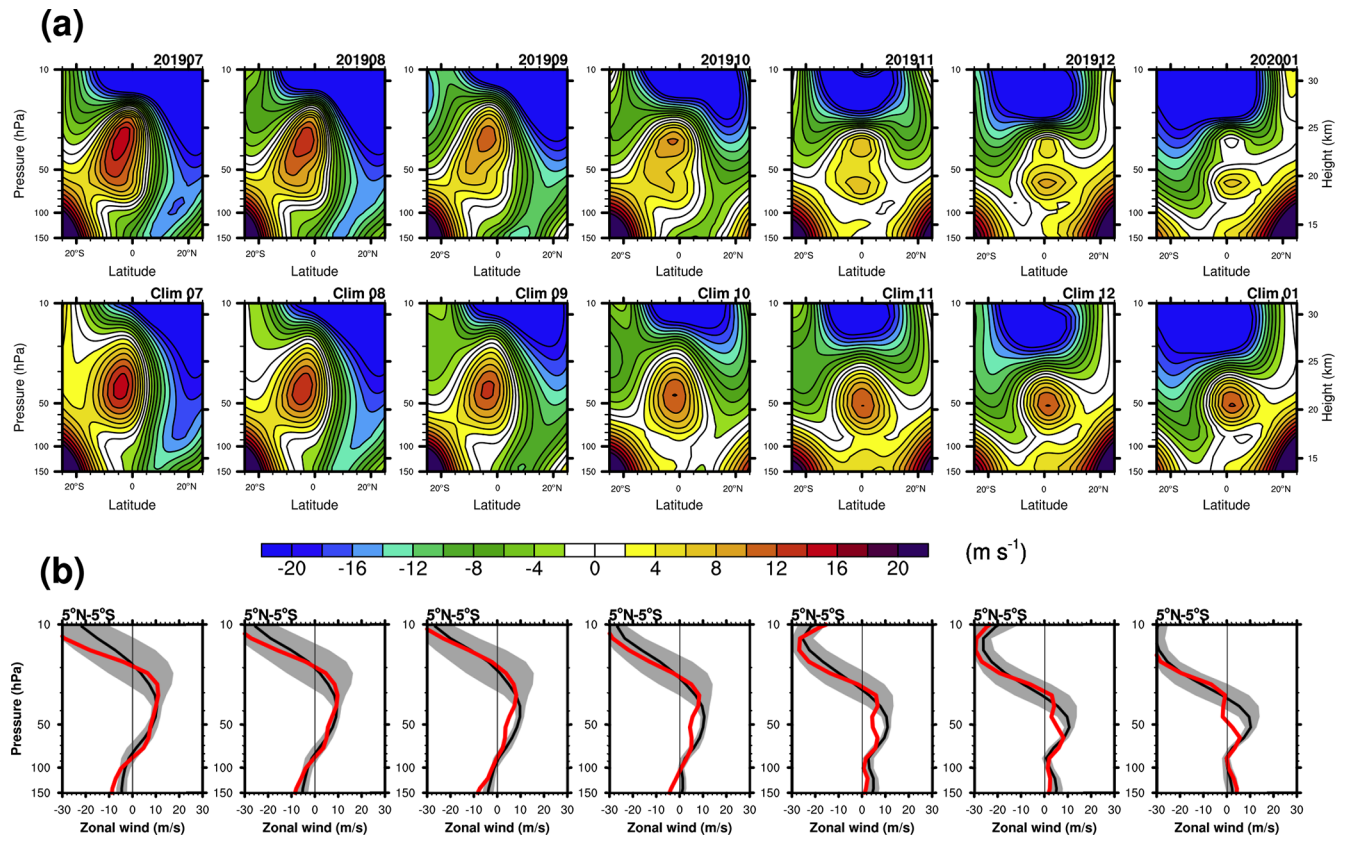

Figure 1. **(a)** Zonal-mean zonal wind in a latitude–height cross section during July–January for the disruption period (2019/20) and **(b)** the climatology. **(b)** Zonal-mean zonal wind averaged for 5° N–5° S during July–January for the disruption period (2019/20; red) and the climatology (black) overlaid with the ±1 SD (gray shading). The climatology corresponds to the westerly QBO years (Sect. 2.1).

ical for inducing the QBO disruption, is anomalously strong at 2–5° N–S compared to the climatology. The MRG waves seem to be mainly generated at the location with positive EPFD at 5–10° N–S and 60–90 hPa, as in the 2015/16 QBO disruption (Fig. 2c of KCG20).

IG wave forcing (Fig. 2d) shows negative values at 10° N–5° S, with an anomalously large magnitude located at 60–80 and 5–15 hPa. Rossby wave forcing (Fig. 2e) is generally strong at altitudes below 50 hPa or poleward of 10° N, but the negative values at 0–5° N at $\sim$ 30 hPa that are stronger than the climatology (magenta stippled) lead to the development of the easterlies at 30–50 hPa; those waves appear to propagate from the NH extratropics.

Figure 3 presents the monthly evolution of the zonal wind, zonal wind tendency, vertical advection (ADVz), required wave forcing (REQ), and each wave forcing averaged for 5° N–5° S from May 2019 to April 2020 at 10–70 hPa. In order to calculate the REQ, both the meridional and vertical advection terms are subtracted from the zonal-mean zonal wind tendency in Eq. (1). From June to September 2019, the magnitude of the WQBO is reduced, without any significant downward propagation (Fig. 3a), compared to the climatology (Fig. 3k). Comparisons between the zonal-mean zonal winds in the 2019/20 QBO disruption and climatology (Fig. 3b) suggest an anomalous weakening of the zonal wind from July 2019, which is maximized at 40–60 hPa. The negative zonal wind tendency near 43 hPa is evident from June to August 2019 (Fig. 3c), which can be mainly attributed to the Rossby wave forcing (Fig. 3j).

The WQBO that maintains its depth without any significant downward propagation in June–September 2019 seems to be related to the strong ADVz (Fig. 3d). ADVz values at 20 hPa in June, July, August, and September 2019 are 9.6, 12.5, 13.3, and 11.3 m s^{-1} per month, respectively, and these values are considerably larger than those for the climatology (2.8, 4.4, 5.8, and 6.3 m s^{-1} per month, respectively; Fig. 3m). In particular, the $\overline{w}^*$ values (Fig. S3) in July and September 2019 are 0.7 and 0.9 mm s^{-1}, respectively, which are 1.6 and 1.5 times larger than that for the climatology, respectively. In this period, midlatitude Rossby wave forcing is extremely large and induces a minor SSW (Anstey et al., 2020; Eswaraiah et al., 2020; Shen et al., 2020), possibly resulting in the enhanced vertical upwelling of the Brewer–Dobson circulation (BDC) and thereby a large magnitude of the ADVz. This implies that the strong ADVz above the altitude at which the disruption occurs can support QBO disrup-

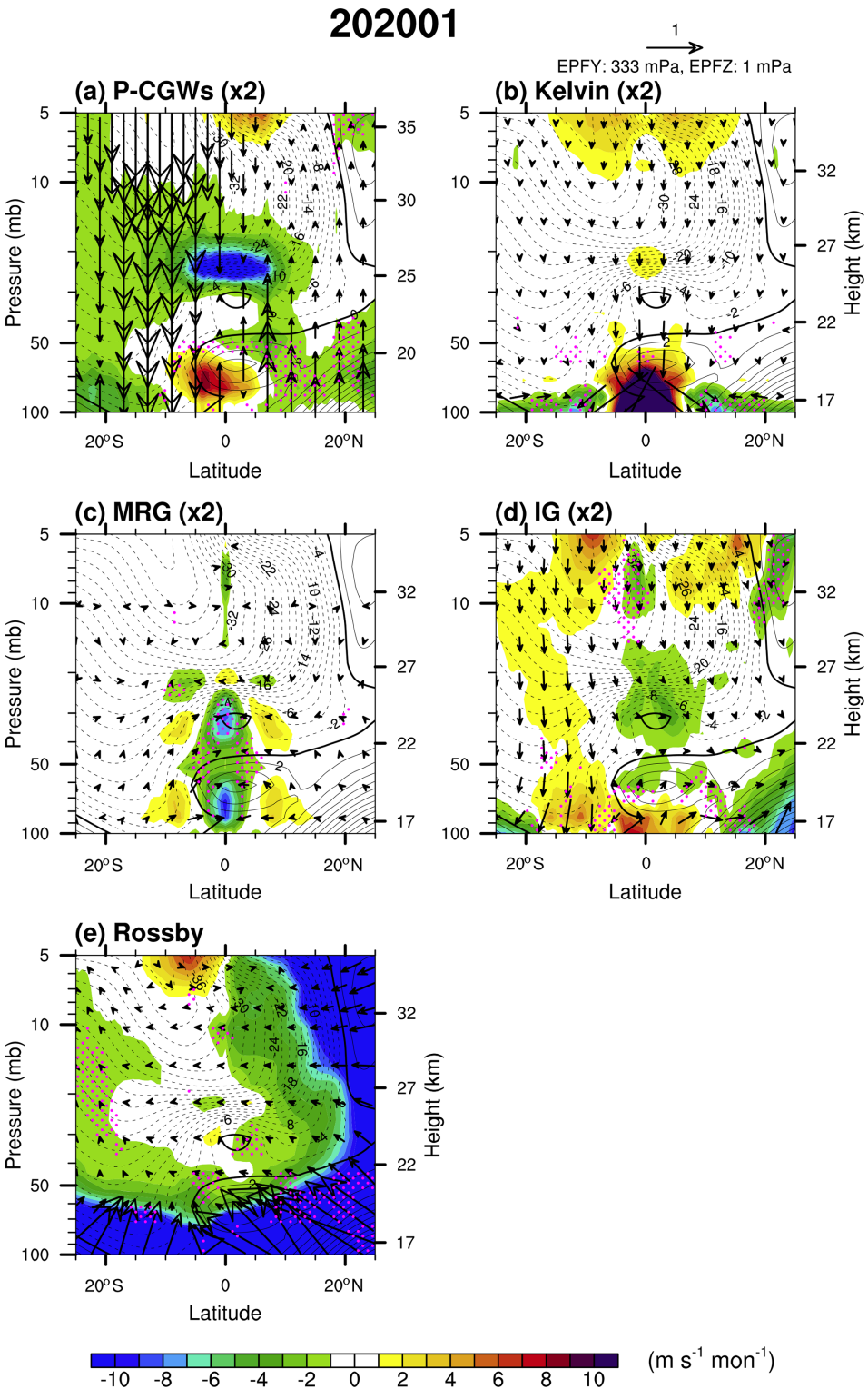

Figure 2. EPF (vectors) and EPFD (shading) in a latitude–height cross section for the **(a)** parameterized CGWs (P-CGWs, multiplied by 2), **(b)** Kelvin waves (multiplied by 2), **(c)** mixed Rossby–gravity waves (MRG, multiplied by 2), **(d)** inertia–gravity waves (IG, multiplied by 2), and **(e)** Rossby waves overlaid with the zonal-mean zonal wind (contour) in January 2020. Solid (dashed) lines indicate westerly (easterly) winds with an interval of 2 m s^{-1}, and thick solid lines indicate a zero zonal wind speed. The magenta stipples represent stronger negative EPFD than the climatology by more than its standard deviation. The reference vector is denoted by an arrow in the upper right corner.

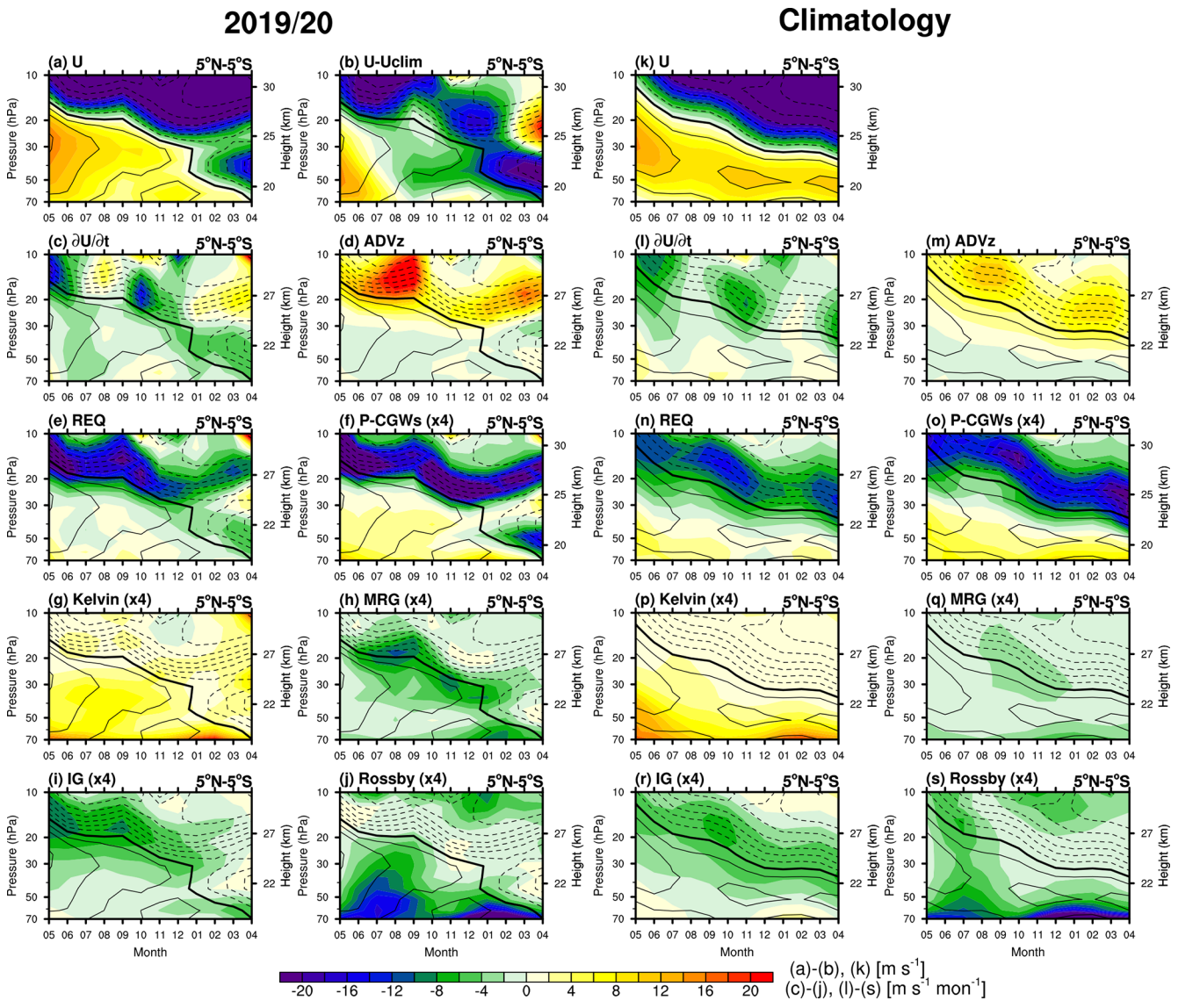

Figure 3. Monthly evolution of the **(a)** zonal-mean zonal wind (U), **(b)** difference in U between the 2019/20 disruption period and the climatology (U − Uclim), **(c)** zonal wind tendency ($\partial U/\partial t$), **(d)** vertical advection (ADVz), **(e)** required wave forcing (REQ), and EPFD for the **(f)** P-CG, **(g)** Kelvin, **(h)**, MRG, **(i)** IG, and **(j)** Rossby waves from May 2019 to April 2020 and **(k–s)** their climatology from May to April from 70 to 10 hPa, superimposed on the zonal-mean zonal wind (black contour lines). The solid (dashed) lines indicate westerly (easterly) winds with an interval of 5 m s^{-1}, and thick solid lines indicate a zero zonal wind speed.

tion by retarding the downward propagation of the WQBO jet. Although the 2019 SSW is classified as a minor SSW in that the zonal-mean zonal wind at 10 hPa at 60° S does not undergo a reversal, the zonal wind at ∼ 32 km at 72° S shows a reversal (Eswaraiah et al., 2020), which implies a strong Rossby wave forcing in the SH.

Climatologically, REQ (Fig. 3n) exhibits a negative (positive) sign in the negative (positive) wind shear zone, and the sign of P-CGW forcing (Fig. 3f) generally follows that of the REQ. The larger the magnitude of the vertical wind shear, the more the P-CGWs explain the REQ. However, in June–July–August (JJA) 2019 (Fig. 3e), a negative REQ is observed at 30–60 hPa without negative vertical wind shear; this seems to be unusual. The P-CGWs start to contribute to the deceleration of the QBO jet after the negative vertical wind shear is generated at ∼ 50 hPa (i.e., October 2019). In contrast to the strong Kelvin wave forcing in the 2015/16 QBO disruption possibly related to El Niño event (Kumar et al., 2018; Li et al., 2020; KCG20), Kelvin wave forcing (Fig. 3g) in the 2019/20 QBO disruption is smaller than or comparable to the climatology (Fig. 3p). This weak Kelvin wave forcing could be one of the reasons why the upper jet at 20–30 hPa is not maintained after the QBO disruption.

During the 2019/20 QBO disruption, the momentum forcing by the MRG waves (Fig. 3h) is considerably stronger than its climatology (Fig. 3q). For instance, from October 2019 to January 2020 the MRG wave forcing at 43 hPa is dominant among the equatorial waves, largely explaining the REQ. This result suggests that MRG waves play a role in reversing the sign of the zonal wind in the later stages. IG wave forcing (Fig. 3i) shows strong negative values in May 2019 above 43 hPa and after July 2019, following the negative wind shear zone. Rossby wave forcing (Fig. 3j) is strong from June to September 2019 below $\sim$ 20 hPa. At 40–50 hPa, Rossby waves continue to provide a negative wave forcing until February 2020.

3.2 Contributions of each wave type at 43 hPa

Figure 4 shows the monthly evolution of zonal wind, zonal wind tendency, and wave forcing of each wave type from May 2019 to April 2020 at 43 hPa; their exact values and percentages are summarized in Table 1. As early as May 2019, the zonal wind tendency (dotted line in Fig. 4a) becomes negative, while in January 2020, the zonal wind (solid line in Fig. 4a) becomes easterly. The negative wind tendency is weakened until October 2019, although it intensifies again in November 2019. The negative wind tendency in May 2019 is mainly explained by the Rossby ($-0.62\,\mathrm{m\,s^{-1}\,mon^{-1}}$) and IG ($-0.57\,\mathrm{m\,s^{-1}\,mon^{-1}}$) waves, with contributions of 48 % and 45 %, respectively. The momentum forcing by the Rossby waves becomes dominant from June to November 2019. The maximum contribution is 82 % (in July 2019), and it decreases subsequently. In December 2019 and January 2020, the MRG wave forcing accounts for 44 % and 41 % of the total negative wave forcing, respectively, which are larger than any other equatorial wave forcing. During the same period, the Rossby wave forcing is the second largest, with contributions of 33 % and 38 %, respectively. In January 2020, parameterized CGWs start to contribute to the easterly development (11 %), and they provide large negative forcing in February 2020 of 44 %.

The meridional and vertical EPFDs of the Rossby waves at 43 hPa are shown in Fig. 4c. In May–September 2019, the meridional component dominates the total Rossby wave forcing, which confirms the strong meridional propagation of Rossby waves from the SH midlatitudes during the austral winter (Anstey et al., 2020). However, in November 2019–February 2020 (i.e., boreal winter) the meridional component becomes weaker, and its magnitude is comparable to that of the vertical component.

In summary, the negative forcing by the Rossby waves contributes most to the zonal wind deceleration from June to September 2019. MRG wave forcing intensifies from October 2019, and it becomes the strongest among all the equatorial wave forcings in December 2019–January 2020. IG waves decelerate the WQBO jet with a moderate magnitude throughout, and the P-CGWs contribute 11 % of the negative forcing in January 2020.

3.3 Rossby waves

Figure 5 shows the latitude–height cross sections of the EPF and EPFD for the Rossby waves and the corresponding meridional and vertical components in July, August, and October 2019 and January 2020. The meridional EPF (EPF-y) values at 10° N and 10° S are presented on the left and right sides of the EPFD-y, respectively, and the vertical EPF (EPF-z) at 70 hPa is presented at the bottom of EPFD-z using red lines. The climatology is represented by black lines, with $\pm 1\sigma$ indicated by the gray shading. In July 2019 (Fig. 5a), the EPFD for the Rossby waves is unusually strong at the northern flank of the QBO at 40–60 hPa. The meridional EPFD dominates the total EPFD at 40–60 hPa in the NH. They are most likely to propagate from the SH based on the large northward EPF at 10° S. Moreover, vertical EPF at 70 hPa is larger than the climatology at 10° N–10° S; accordingly, a large negative EPFD-z can be observed at 30–50 hPa. In August 2019 (Fig. 5b), there is evident deceleration of the WQBO jet by the Rossby waves propagating from the SH; however, the negative wave forcing becomes stronger at the jet core. It is also found that the EPF-z at 70 hPa in August 2019 is larger than that in July 2019 at 5° N–20° S.

In October 2019 (Fig. 5c), the shape of the zonal wind is significantly deformed by the anomalously strong negative forcing in the WQBO jet, mainly attributed to the strong meridional Rossby wave forcing originating from the SH. In January 2020 (Fig. 5d), when the QBO disruption occurs, the Rossby wave forcing is generally weaker than that shown in Fig. 5a–c; consequently, the EPFD in Fig. 5d is multiplied by a factor of 2. The Rossby waves laterally propagating from the NH decelerate an isolated small westerly jet at 30–40 hPa, while the vertically propagating Rossby waves provide an anomalously strong easterly forcing below the altitude of 40 hPa at 25° N–15° S, except close to the Equator. The EPF-z at 70 hPa, which is larger during the disruption period than the climatology at 0–20° S and 10–20° N, confirms the presence of the strong Rossby waves propagating from the equatorial region.

In summary, Rossby wave forcing and flux during the austral winter of 2019 have a dominant meridional component propagating from the SH. However, a relatively small magnitude of the Rossby wave forcing is found with comparable meridional and vertical components in January 2020. The strong EPF-z at 70 hPa mostly propagates from the equatorial troposphere and the NH when the EPF is traced back to the troposphere (Fig. S4 in the Supplement).

As mentioned previously, a minor SSW took place in the SH in September 2019, which was an exceptionally rare event. This implies that Rossby wave flux and forcing in the midlatitude stratosphere were above average during the austral winter of 2019. Figure 6 shows the latitude–height

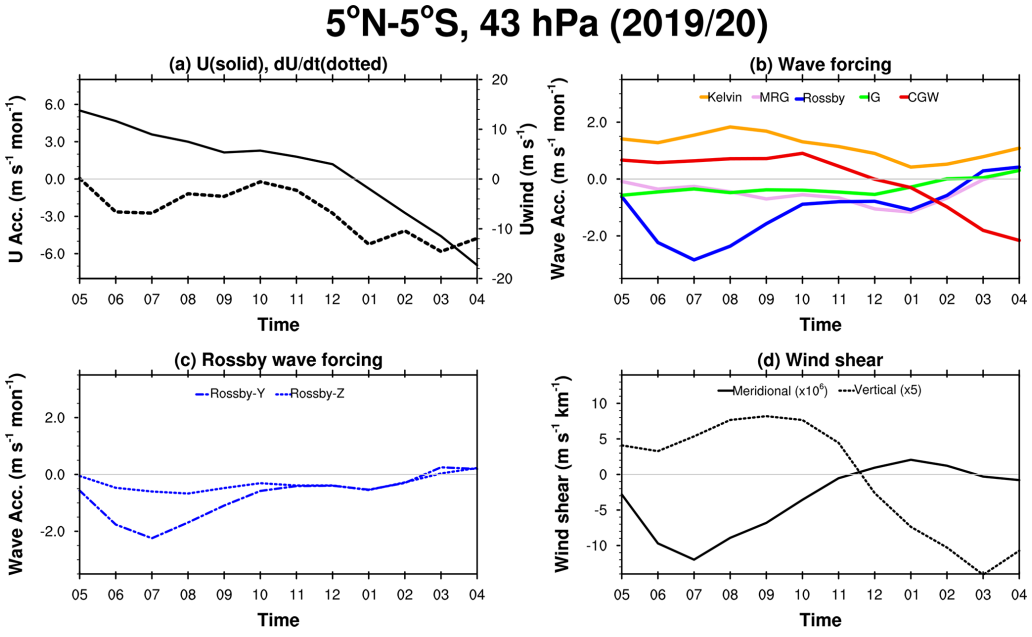

Figure 4. Monthly evolution of the **(a)** zonal-mean zonal wind (solid) and zonal wind tendency (dotted), **(b)** momentum forcing by the Kelvin waves (orange), MRG waves (pink), Rossby waves (blue), IG waves (light green), and CGWs (red) averaged over 5° N–5° S (dotted) at 43 hPa from May 2019 to April 2020. **(c)** Momentum forcing by the Rossby waves decomposed into the meridional (dot-dashed) and vertical components (dotted). **(d)** Meridional wind shear across the Equator (solid) and vertical wind shear (dotted).

Table 1. Monthly averaged momentum forcing by each wave type ($m\,s^{-1}$ per month) at 43 hPa averaged for 5° N–5° S from June to January for the disruption period (2019/20) and the climatology. The ratio of each wave forcing to the total negative forcing is given in parentheses only when the wave forcing is negative.

2019/20	Jun 2019	Jul 2019	Aug 2019	Sep 2019	Oct 2019	Nov 2019	Dec 2019	Jan 2020
MRG	−0.4 (12 %)	−0.3 (8 %)	−0.4 (14 %)	−0.7 (27 %)	−0.6 (30 %)	−0.7 (34 %)	−1.1 (44 %)	−1.2 (41 %)
IG	−0.5 (15 %)	−0.3 (10 %)	−0.5 (15 %)	−0.4 (14 %)	−0.4 (21 %)	−0.5 (24 %)	−0.5 (23 %)	−0.3 (10 %)
Rossby	−2.2 (73 %)	−2.8 (82 %)	−2.4 (71 %)	−1.6 (59 %)	−0.9 (49 %)	−0.8 (42 %)	−0.8 (33 %)	−1.1 (38 %)
CGW	0.6	0.6	0.7	0.7	0.9	0.5	−0.01 (0 %)	−0.3 (11 %)
Kelvin	1.3	1.5	1.8	1.7	1.3	1.1	0.9	0.4
Rossby-Y	−1.8 (58 %)	−2.2 (65 %)	−1.7 (51 %)	−1.1 (41 %)	−0.6 (32 %)	−0.4 (22 %)	−0.4 (17 %)	−0.5 (19 %)
Rossby-Z	−0.5 (15 %)	−0.6 (17 %)	−0.7 (20 %)	−0.5 (18 %)	−0.3 (17 %)	−0.4 (20 %)	−0.4 (16 %)	−0.5 (19 %)
Climatology	Jun	Jul	Aug	Sep	Oct	Nov	Dec	Jan
MRG	−0.2 (16 %)	−0.1 (5 %)	−0.1 (5 %)	−0.1 (10 %)	−0.2 (19 %)	−0.4 (23 %)	−0.5 (20 %)	−0.4 (19 %)
IG	−0.1 (9 %)	−0.3 (15 %)	−0.3 (18 %)	−0.4 (33 %)	−0.7 (54 %)	−0.9 (48 %)	−0.9 (39 %)	−0.8(36 %)
Rossby	−1.2 (75 %)	−1.7 (80 %)	−1.4 (77 %)	−0.7 (57 %)	−0.3 (27 %)	−0.4 (24 %)	−0.6 (26 %)	−0.7 (34 %)
CGW	1.0	0.8	0.6	0.6	0.4	−0.1 (5 %)	−0.3 (14 %)	−0.2 (11 %)
Kelvin	2.2	1.3	1.0	0.9	0.7	0.5	0.6	0.7
Rossby-Y	−1.1 (72 %)	−1.6 (74 %)	−1.2 (70 %)	−0.6 (51 %)	−0.1 (12 %)	0.0 (0 %)	−0.0	−0.1 (5 %)
Rossby-Z	−0.1 (3 %)	−0.1 (6 %)	−0.2 (7 %)	−0.1 (6 %)	−0.2 (15 %)	−0.4 (24 %)	−0.6 (26 %)	−0.6 (29 %)

cross section of the EPF overlaid with the zonal-mean zonal wind (Fig. 6a), vertical EPF at 100 hPa (Fig. 6b), and zonal wind at 15° S (Fig. 6c) in JJA. The red line represents the 2019 case, and the black line represents the climatology. The waves are generally vertically propagating, while a part of the waves propagates into the tropics. The vertical EPF penetrating the stratosphere is considerably larger than the climatology by $\sim 2\sigma$ (Fig. 6b). An excessively large EPF in the midlatitude stratosphere could also propagate into the Equator because the zonal-mean zonal wind in the SH subtropics at 40–80 hPa exhibits stronger westerly winds than the climatology (Fig. 6c).

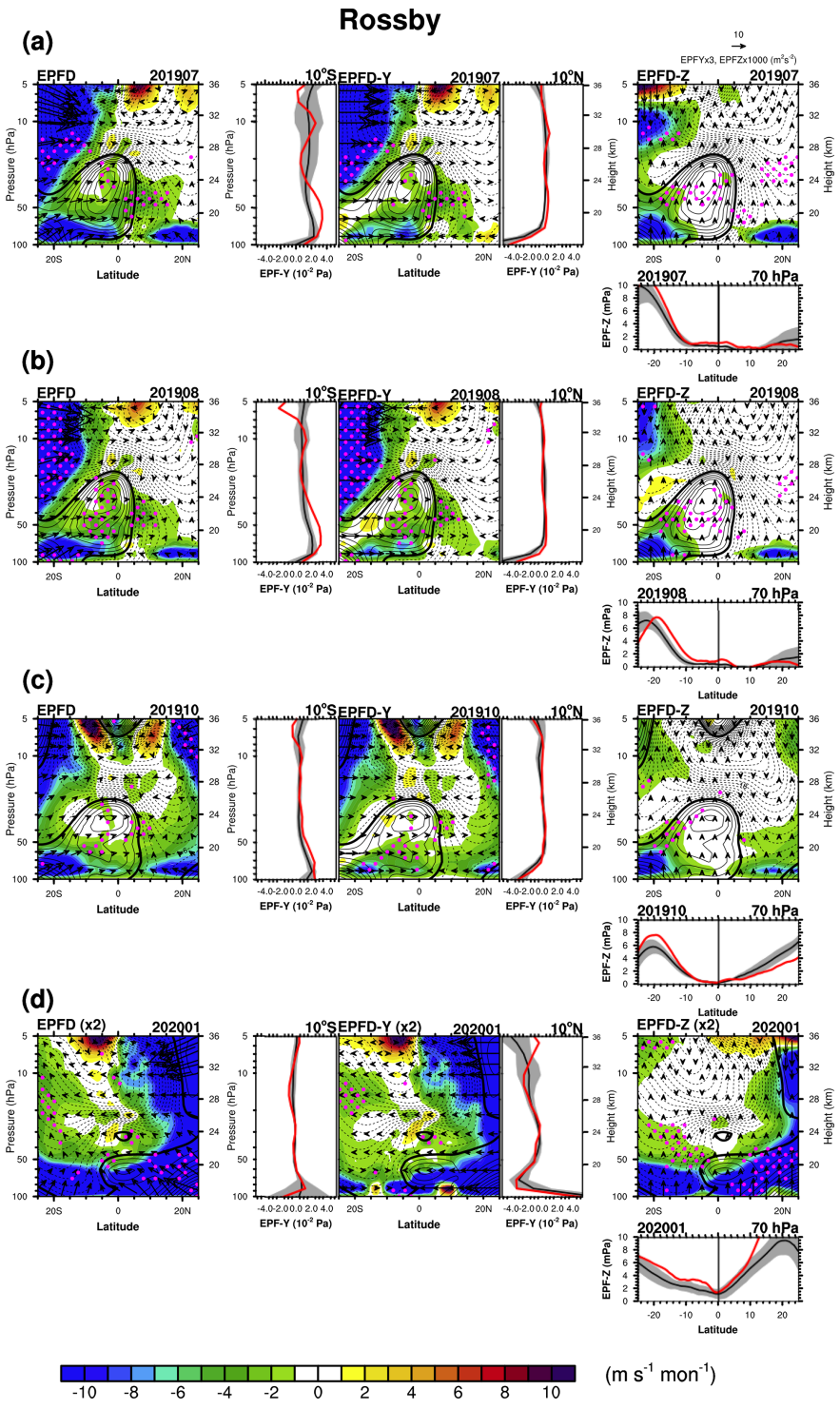

Figure 5. EPF divided by air density (first column; vectors) and EPFD (shading) for the Rossby waves in a latitude–height cross section, along with (second column) their meridional and (third column) vertical components in **(a)** July 2019, **(b)** August 2019, **(c)** October 2019, and **(d)** January 2020. The vertical profiles of the meridional EP fluxes at 10° S and 10° N are presented on the left and right sides of the EPFD-y, and the meridional distribution of the vertical EP flux at 70 hPa is presented at the bottom of the EPFD-z (red and black lines correspond to the disruption and the climatology, respectively, with ± 1 SD; gray shading). The solid (dashed) lines indicate westerly (easterly) winds with an interval of $2\,\mathrm{m\,s^{-1}}$, and thick solid lines indicate a zero zonal wind speed. The magenta stipples represent stronger negative EPFD than the climatology by more than its standard deviation.

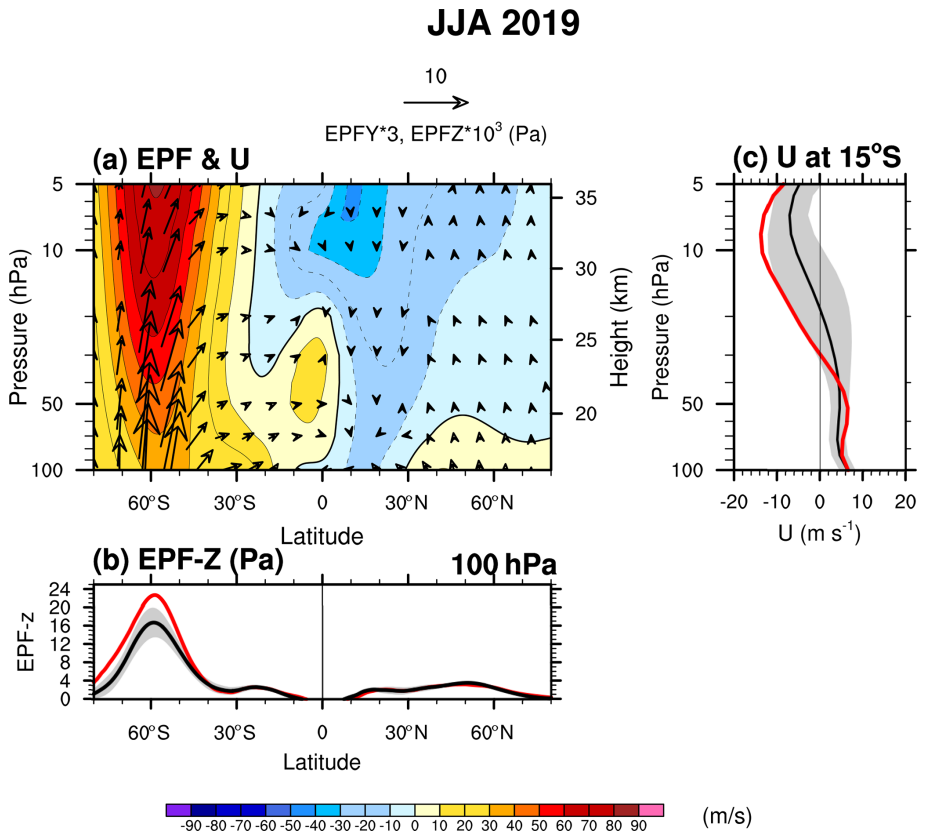

Figure 6. **(a)** EPF vectors superimposed on the zonal-mean zonal wind (contour) in a latitude–height cross section, **(b)** vertical component of the EPF at 100 hPa, and **(c)** zonal-mean zonal wind profile at 15° S in June–July–August (JJA) 2019 (red) and JJA climatology for WQBO (black) with ±1 SD (gray shading).

3.4 MRG waves

Figure 7 shows the EPF and EPFD similar to Fig. 5 but for the MRG waves in October, November, and December 2019 and January 2020. In October 2019 (Fig. 7a), the MRG waves exert strong negative forcing, especially at 20–50 hPa between 5° N and 5° S and at 10–40 hPa between 5 and 10° N. The negative MRG wave forcing at 30–50 hPa near the Equator, which is strongly related to the QBO disruption, seems to propagate from the regions with positive EPFD: (i) 60–80 hPa at 5–10° N, (ii) 40–80 hPa near 10° N, and (iii) ∼ 40 hPa near 10° S. This is supported by considerably stronger vertical EPF at 70 hPa at 0–10° N and meridional EPF at 20–50 hPa at 10° N–S. In November 2019 (Fig. 7b), similar features as in October 2019 are shown but with a reduced vertical range for the negative wave forcing near the Equator.

In December 2019 (Fig. 7c), westerly winds at 30–50 hPa are weakened. The negative MRG wave forcing becomes unusually strong at 50 hPa in the 5–10° S range, although the increase in the EPF-z at 70 hPa is smaller than those in October and November 2019. In January 2020 (Fig. 7d), MRG wave forcing at 43 hPa is the largest among all the equatorial wave forcings. Not only the equatorward waves at 10° N–S at 30–50 hPa but also the equatorward and upward waves at 10° N–S at 70 hPa are much stronger than the climatology by more than 1σ. In particular, the upward and equatorward EPF vectors starting from 5–10° S at 70 hPa appear to exhibit the maximum contribution to the negative forcing observed at 43 hPa.

Figure 7 shows that the MRG waves weaken the QBO jet and finally reverse the wind sign in the later period (e.g., December 2019 and January 2020). The negative MRG wave forcing is exerted on the jet core not only at the 43 hPa altitude but also at the altitude range of 25–50 hPa, resulting in an excessive weakening of the upper jet (∼ 30 hPa) during the 2019/20 QBO disruption. In addition, MRG waves are strongly generated in regions with a large horizontal wind curvature, coincident with the location of the positive EPFD. Therefore, in order to investigate whether the MRG waves are generated by barotropic and baroclinic instability, we select two regions (boxed regions in Fig. 8) with small positive $\overline{q}_\phi$ values. One of the two boxes is located in a similar place as the box in KCG20 (10–15° S, 60–90 hPa), and the other is located at 10–15° N and 60–90 hPa.

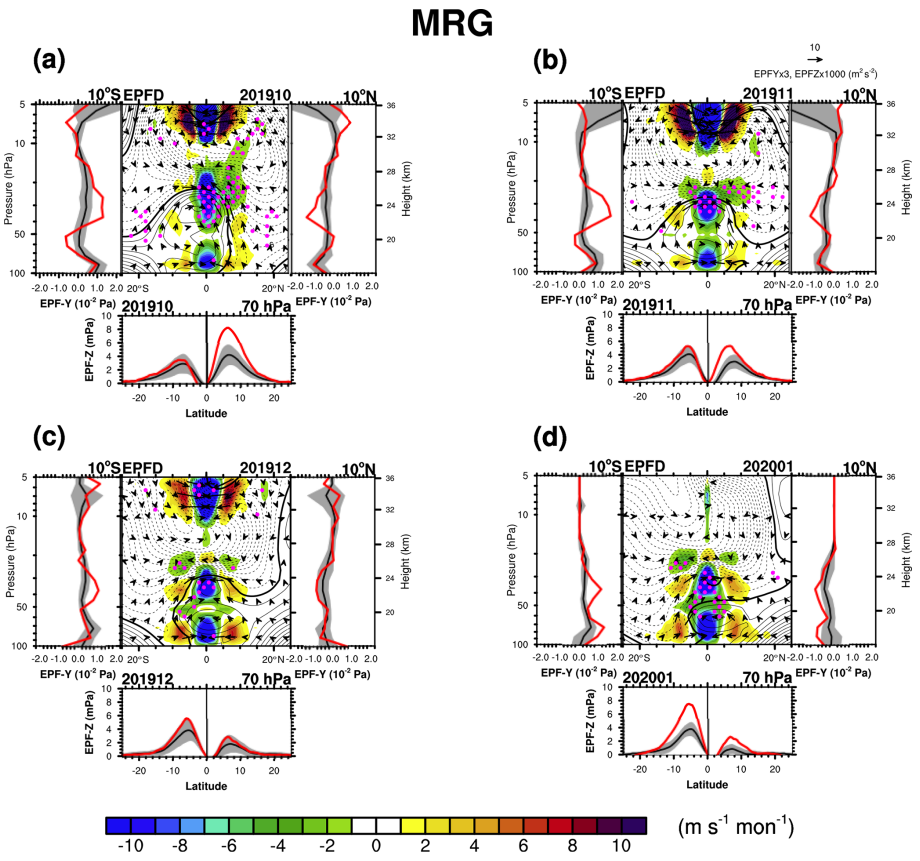

Figure 7. EPF divided by air density (vectors) and EPFD (shading) for the MRG waves multiplied by 8 and 4, respectively, in a latitude–height cross section in **(a)** October 2019, **(b)** November 2019, **(c)** December 2019, and **(d)** January 2020. The vertical profiles of the meridional EP fluxes at 10° S (10° N) are presented on the left and right sides of the EPFD, and the meridional distribution of the vertical EP flux at 70 hPa is presented at the bottom of the EPFD. Contours and the magenta stipples are defined the same as those in Fig. 5.

Figure 8 shows the monthly averaged $\overline{q}_\phi$ and the daily time series of the number of grids with the negative $\overline{q}_\phi$ for the boxed region in December 2019 (Fig. 8a and c) and January 2020 (Fig. 8b and d), along with the climatology. Note that the total number of grids in the boxed region is 33. The monthly mean $\overline{q}_\phi$ in the boxed region shows small positive values in December 2019 and in January 2020; however, the number of negative $\overline{q}_\phi$ in the boxed region based on the daily mean values (Fig. 8c and d) is generally much larger during the disruption period compared to that of the climatology. In the boxed region, meridional curvature term (second term of Eq. 3) dominates $\overline{q}_\phi$; on that basis barotropic instability in the boxed region is likely to generate anomalously strong MRG waves.

The zonal mean precipitation in the tropical region from June 2019 to January 2020 (Fig. S5) is comparable to the climatology, except in June and October 2019 at 5° N–5° S, showing greater precipitation than the climatology by $\sim 1\sigma$. Now we examine the precipitation spectrum in association with the equatorial wave mode during the 2019/20 disruption. Figure 9 shows 10° S to 10° N averaged precipitation spectrum as a function of zonal wavenumber (k) and frequency (ω), divided by the background spectrum for the symmetric (a and c) and antisymmetric (b and d) components with respect to the Equator from October 2019 to January 2020. The background spectrum of the symmetric (antisymmetric) component is obtained by applying 1–2–1 smoothing for k and ω 40 and 10 times, respectively, to the raw symmetric (antisymmetric) spectrum (see KCG20). Following Wheeler and Kiladis (1999), the values greater than 1.4 in Fig. 9 are considered statistically significant wave signals at the 95 % confidence level. The areas of the spectrum where values are more than 1σ stronger than the climatology (blue-stippled pattern) and the precipitation spectrum divided by its background spectrum is larger than 1.4 start to widen in December 2019, although the area is smaller than that in the 2015/16 QBO disruption. Generally, areas of strong power that are evident in the spectrum are related to the Kelvin and IG waves. In the symmetric spectrum, statistically significant Rossby wave signals ($k = -16$–19, $\omega = 0.06$–0.1 cpd) are shown, which are stronger than the climatology by more than 1σ in November 2019–January 2020 (Fig. 9b–d). The enhancement of the Rossby waves in the troposphere in January 2020 probably affects the large vertical EPF at 70 hPa

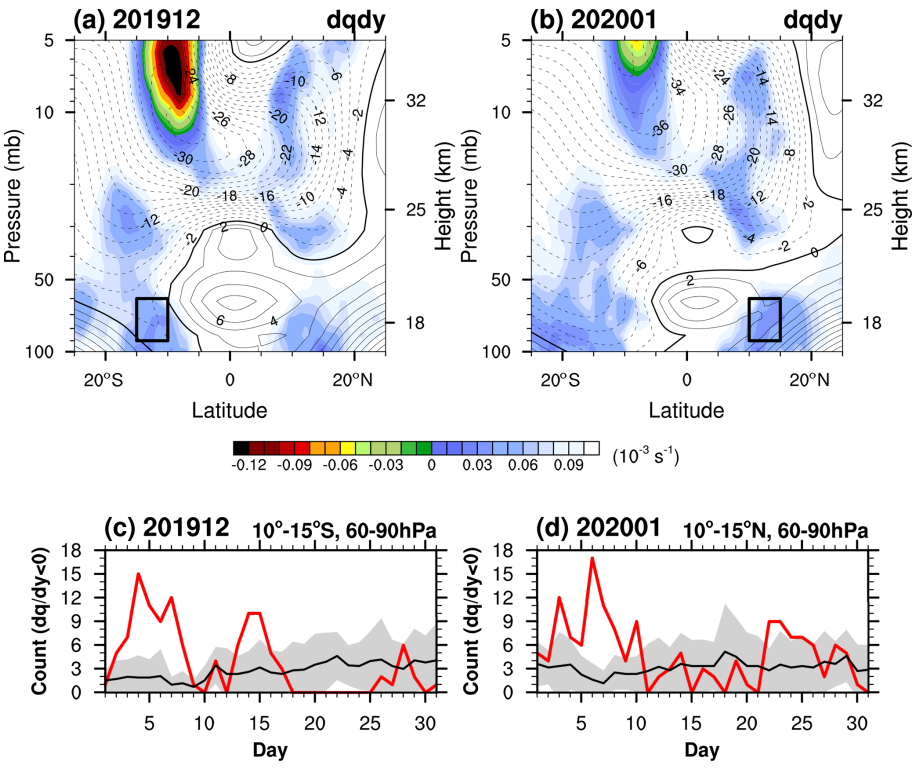

Figure 8. Monthly averaged meridional potential vorticity gradient in a latitude–height cross section (shading) overlaid with the zonal-mean zonal wind (contour) in **(a)** December 2019 and **(b)** January 2020. The solid (dashed) lines indicate westerly (easterly) winds with an interval of 2 m s^{-1}, and thick solid lines indicate a zero zonal wind speed. Time series of the number of grids with negative daily mean $\overline{q}_{\phi}$ (s^{-1}) in the **(c)** boxed region in the SH (10–15° S, 60–90 hPa) in December 2019 and **(d)** that in the NH (10–15° N, 60–90 hPa) in January 2020 (red). The black lines in Fig. 8c and d correspond to the climatology with ±1 SD (gray shading).

(Fig. 5d). Kelvin wave signals ($k = 0$–8 and $\omega = 0$–0.25) are statistically significant throughout and are more than 1σ stronger than the climatology after November 2019. It is likely that these waves propagate to the stratosphere and thereby contribute to the strong EPF-z at 70 hPa (see Fig. S1). In the antisymmetric spectrum, the MRG wave signals in the antisymmetric spectrum ($k = -10$–0 and $\omega = 0.2$–0.32) are stronger than the climatology by more than 1σ in December 2019–January 2020. Therefore, the enhanced convective activity in the MRG wave spectrum in December 2019–January 2020, together with the barotropic instability at the QBO edges, may affect the anomalously strong MRG wave forcing near 43 hPa. Overall, convectively coupled equatorial waves are slightly enhanced in the later period of the 2019/20 QBO disruption, although the zonal mean precipitation is not significantly increased.

3.5 IG waves

Figure 10 shows the EPF and EPFD as a function of latitude and height, as well as the latitudinal distribution of the vertical EPF by the IG waves at 70 hPa from October 2019 to January 2020. Given that IG waves generally propagate upward in the stratosphere, the upward-directed EPF vectors inside the WQBO jet at 5° N–5° S indicate a larger magnitude of the westward IG waves compared to that of the eastward IG waves. The negative IG wave forcing is exerted on the jet core throughout, with a significant magnitude located at the altitude range of 60–90 hPa. However, the magnitude of the EPF-z at 70 hPa is slightly larger than that of the climatology in December 2019 and January 2020, differing from the case in the 2015/16 QBO disruption in that the EPF-z at 70 hPa was significantly larger than the climatology.

Figure 11 illustrates the 10° S to 10° N averaged phase-speed spectrum of the precipitation for the IG wave ranges, which approximately represents the source spectrum of the IG waves in December 2019 (Fig. 11a) and January 2020 (Fig. 11b), along with the climatology. Generally, the disruption period shows a larger IG wave source spectrum by $\sim 1\sigma$ compared to the climatology. The zonal wind speed at 140 hPa is approximately 2.6 and 4.9 m s^{-1} in December 2019 and the climatology, respectively. Therefore, the IG source spectra during both the disruption period and climatology exhibit dominant westward components, although the climatology exhibits additional westward waves at a phase speed of 2.6–4.9 m s^{-1}. However, the additional westward waves of the climatology at 2.6–4.9 m s^{-1} are dissipated by

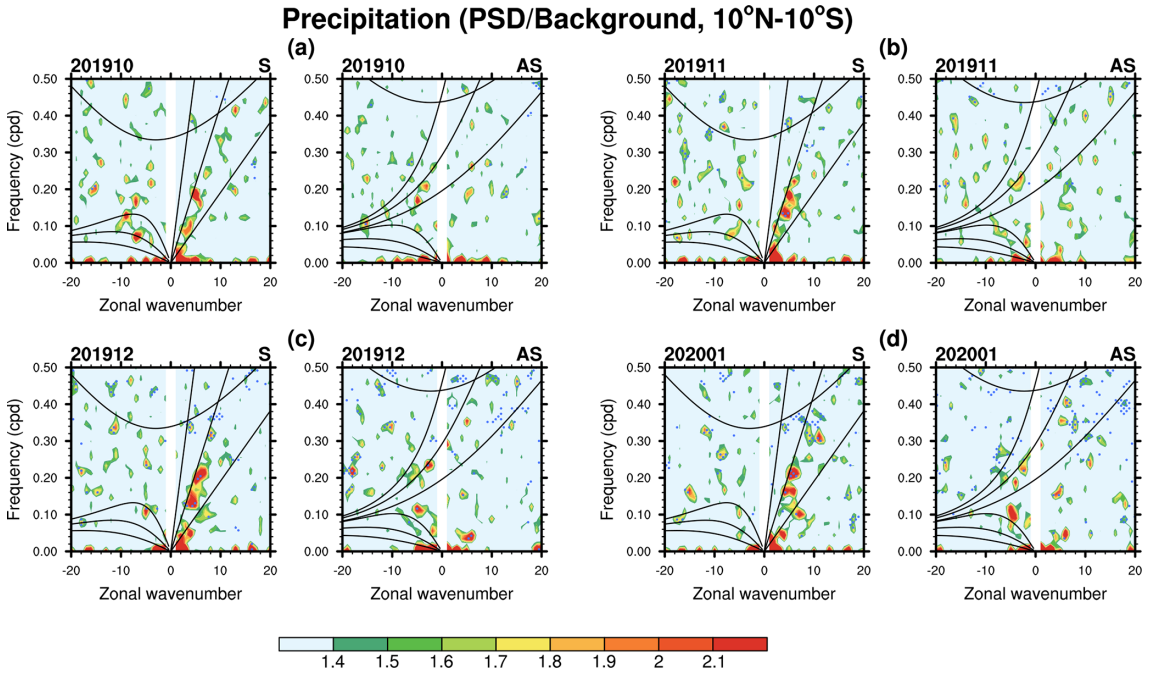

Figure 9. Zonal wavenumber–frequency spectra of the MERRA-2 precipitation divided by that of the background spectrum for **(a, c)** the symmetric and **(b, d)** antisymmetric components (separately) averaged between 10° N and 10° S for **(a)** October 2019, **(b)** November 2019, **(c)** December 2019, and **(d)** January 2020. The value larger than 1.4 is statistically significant at the 95 % confidence level using a t test. The blue stipples represent power spectral density (PSD) greater than the climatology by more than its standard deviation. The theoretical dispersion relation for each equatorial wave mode is denoted by a black solid line for the equivalent depths of $h = 8$, 40, and 240 m, but for the IG waves only the $h = 8$ m line is shown.

the critical-level filtering (-0.2–$5.4\,\mathrm{m\,s^{-1}}$), and this range is wider than that (1.1–$4.2\,\mathrm{m\,s^{-1}}$) of the disruption period. Thus, the remaining westward waves at 70 hPa are stronger in December 2019 than the climatology. The narrower critical-level filtering range is related to the westerly anomalies and easterly anomalies at 70–100 and 100–140 hPa, respectively (Fig. S6 in the Supplement). In January 2020, compared to the climatology, the estimated IG spectrum at the source level exhibits additional westward waves at 2.2–$4.4\,\mathrm{m\,s^{-1}}$ due to the stronger westerlies at the source level (Fig. S6). Despite these waves being almost filtered by the critical-level filtering process, the eastward shift of the critical-level filtering range compared to the climatology results in more westward waves remaining at the altitude of 70 hPa. In addition, the eastward waves in the climatology are less filtered than those during the disruption period. The findings shown in Fig. 11 indicate that slightly stronger westward IG waves at 70 hPa during the disruption period can be explained by the narrow critical-level filtering range for the westward IG waves and the enhanced convective activity. This conclusion is similar to that regarding the IG waves during the 2015/16 QBO disruption.

3.6 Parameterized CGWs

Figure 12 presents the 5° N–5° S averaged zonal-mean zonal wind as well as the convective gravity wave drag (CGWD; a and b) and the source-level CGW momentum flux (i.e., cloud-top momentum flux; CTMF) (c and d) in January 2020, along with the climatology. At pressures above 40 hPa the maximum negative CGWD of $-0.7\,\mathrm{m\,s^{-1}}$ per month is shown at 47 hPa, where there is negative vertical wind shear. This magnitude is less than half of the maximum negative CGWD in February 2016. The westward-propagating CTMF is comparable to the climatology, consistent with the small negative CGWD.

Figure 13 shows the convective source spectrum and the wave-filtering and resonance factor (WFRF) spectrum in January 2020 as well as the climatology. As mentioned in KCG20, the CTMF spectrum is derived based on the spectral combination of the convective source spectrum and the WFRF (see Eq. 1 of Kang et al., 2017). The convective source spectrum is amplified at the phase velocity equal to the convection moving speed (c_{qh}), and its overall magnitude is dependent on the square of the convective heating rate. The following effects are included in the WFRF: (i) critical-level filtering within the convection and (ii) resonance between the vertical harmonics constituting convective forcing and the natural wave modes given by the dispersion relation-

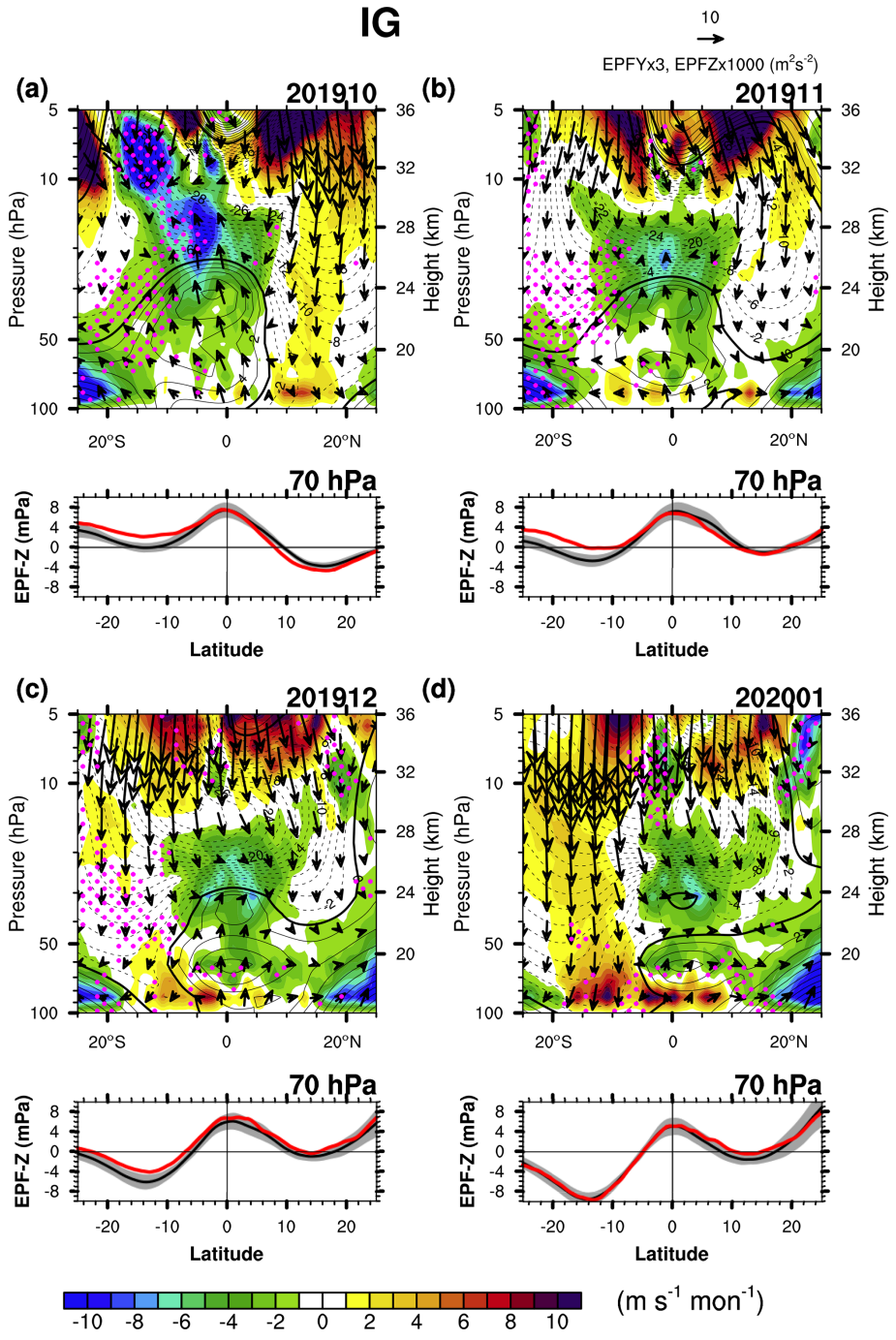

Figure 10. EPF divided by air density (vectors) and EPFD (shading) for the IG waves multiplied by 4 in a latitude–height cross section with the (bottom) meridional distribution of the vertical EP flux at 70 hPa in **(a)** October 2019, **(b)** November 2019, **(c)** December 2019, and **(d)** January 2020 (red) as well as the corresponding monthly climatology (black) with ±1 SD (gray shading). Contours and the magenta stipples are defined the same as those in Fig. 5.

ship (Song and Chun, 2005; KCG20). The convective source spectrum (Fig. 13a) is slightly stronger than that for the climatology owing to the slightly stronger convection during the disruption. The WFRF (Fig. 13b) is also slightly stronger with a slightly wider spectrum than that for the climatology at 5° N–5° S. Therefore, both the convective source spectrum and WFRF lead to a somewhat stronger CTMF compared to the climatology. Furthermore, as 2019 was recorded as the second-warmest year (GISTEMP, 2020), global warming likely led to higher static stability at the cloud top and hence

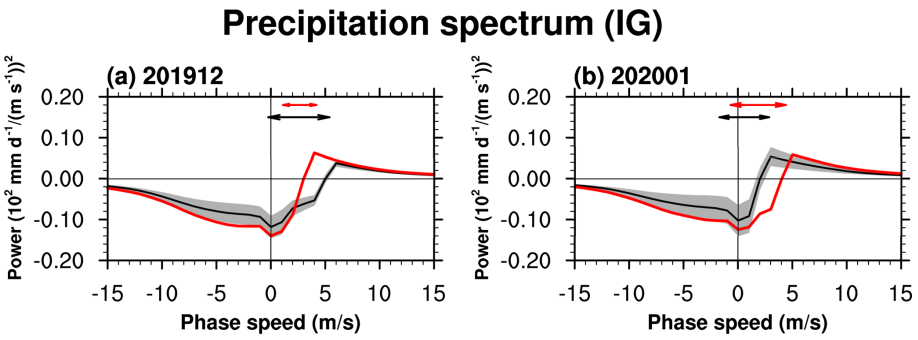

Figure 11. The 10° S to 10° N averaged precipitation spectrum for the IG wave range [(i) $|k| > 20$ and $\omega > 0$ cpd or (ii) $|k| \leq 20$ and $\omega > 0.4$ cpd] as a function of phase speed in **(a)** December 2019 and **(b)** January 2020 along with the corresponding monthly climatology (black) and ±1 SD (gray shading). The spectrum with a negative sign represents the westward-propagating waves. Double-sided arrows in the upper part of each panel indicate the zonal wind ranges between 140 hPa (i.e., source level) and 70 hPa for the QBO disruption period (red) and climatology (black).

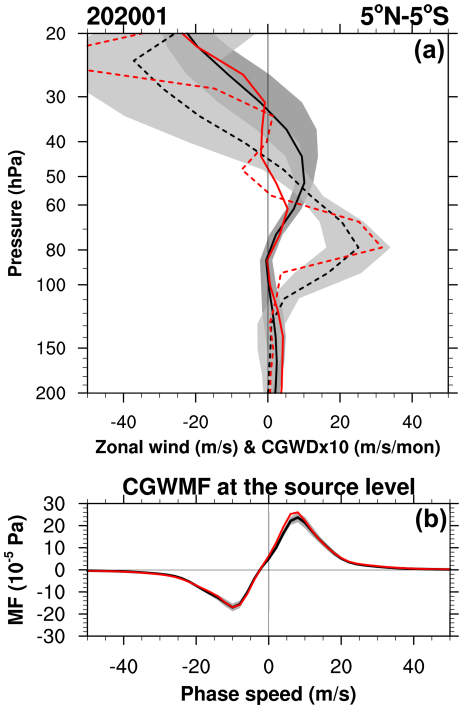

Figure 12. (a) Vertical profiles of the zonal-mean zonal wind (red solid) and zonal mean CGWD (red dashed) averaged for 5° N–5° S in January 2020 and those for the climatology (black solid and black dashed, respectively) with ±1 SD (dark-gray and light-gray shading, respectively). **(b)** The zonal-mean zonal CGW momentum flux spectrum at the cloud top averaged for 5° N–5° S in January 2020 (red) and its climatology (black) with ±1 SD (gray shading).

to the strong CTMF. This is because the CTMF generally increases as the stability increases due to the proportionality of the stability at and above the cloud top to the CTMF (N_2 is proportional to $\overline{M}_c$ in Eq. 22 in Song and Chun, 2005). However, the enhancement of the CTMF by CGWs in 2019/20 is much smaller than that in the 2015/16 QBO disruption, which can be partly attributed to the strong El Niño in the 2015/16 winter.

In Fig. 13, white and gray line represents the zonal wind at the cloud top (U_{ct}) and the moving speed of convection (c_{qh}), respectively. The U_{ct} averaged for 5° N–5° S exhibits a weaker easterly ($-3.0\,m\,s^{-1}$) compared to the climatology ($-4.5\,m\,s^{-1}$). In addition, c_{qh} exhibits a weaker easterly ($-2.1\,m\,s^{-1}$) compared to the climatology ($-2.8\,m\,s^{-1}$). The eastward shifts of the zonal wind at the cloud top and c_{qh} cause stronger westward and eastward momentum fluxes, respectively; the competition between the two factors results in an increased eastward momentum flux (Fig. 12b). In our CGW parameterization, we obtain c_{qh} by averaging the zonal wind below 700 hPa, which is related to the propagation speed of the gust front (Choi and Chun, 2011). Therefore, the westerly anomalies in c_{qh} are caused by the westerly anomalies in the zonal wind below 700 hPa. The westerly anomalies in the lower troposphere are often found in future climate simulations (Collins et al., 2010), but there is a need for further study on the cause and significance of the westerly anomalies in a warmer climate, although doing so is beyond the scope of this study. Although the magnitude of the westward CGWs at the source level is similar to that in the climatology, the eastward shift of the zonal winds at 100–200 hPa (Fig. 12) resulted in more westward waves propagating into the stratosphere compared to those in the climatology. Overall, the increase in the CGW momentum flux in January 2020 is considerably smaller than that in February 2016, and no significant increase is observed in the westward momentum flux. Together with the weaker negative vertical wind shear at 43 hPa, this results in a small magnitude of the negative CGW forcing near 43 hPa.

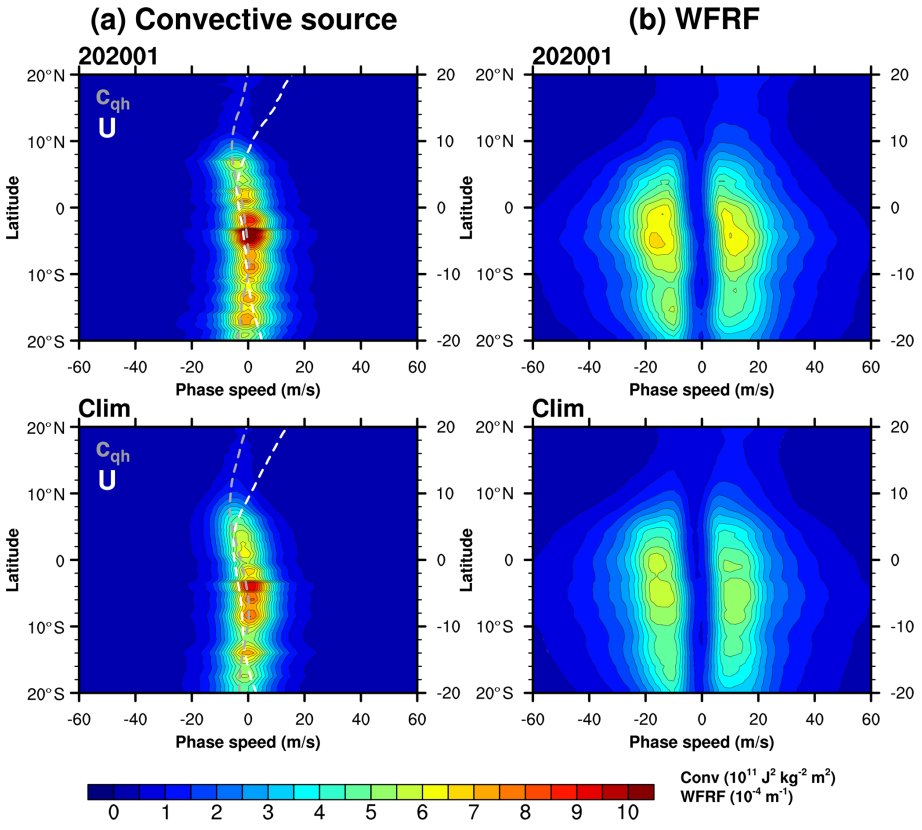

Figure 13. Phase-speed spectrum of the **(a)** convective source and **(b)** wave-filtering and resonance factor (WFRF) in (top) January 2020 and (bottom) and its climatology as a function of the latitude between 20° N and 20° S. Zonal-mean zonal wind at the cloud top (U_{ct}) and moving speed of convection (c_{qh}) are denoted by white and gray dashed lines, respectively, in the convective source spectrum.

3.7 Differences between 2015/16 and 2019/20 QBO disruptions

There are two major differences between the 2015/16 and 2019/20 QBO disruptions. First, the 2019/20 QBO disruption exhibited weaker and thinner westerly winds near 30 hPa than the 2015/16 one. Therefore, at first glance, the 2019/20 QBO disruption appears to be a normal QBO propagating downward with time. This is because Rossby waves propagating from the SH midlatitudes, which induce a localized wind deceleration, were the strongest in the early stage of the 2019/20 QBO disruption (Fig. 4), and vertically propagating MRG wave forcing mainly induced the wind reversal in the later stage of the 2019/20 QBO disruption. Furthermore, the large magnitude of the MRG wave forcing resulted in a deceleration of the entire westerly jet above the altitude of 43 hPa. This is different from the 2015/16 QBO disruption in that the MRG waves initiate the disruption by providing a localized forcing, and then the Rossby waves finalize the QBO disruption. Another reason for the weaker and thinner westerly winds at 20–30 hPa is a relatively shallower QBO depth and weaker positive wave forcing by Kelvin waves and eastward CGWs during the 2019/20 QBO disruption (Fig. S2 in the Supplement) than during the 2015/16 QBO disruption (Fig. S3 of KCG20). However, it is not clear whether the weak positive wave forcing causes the weak vertical wind shear or weak vertical wind shear causes the weak positive wave forcing. Nevertheless, the fact that both Kelvin waves propagating from the troposphere (Fig. S1) and CGWs at the source level (Fig. 12) were less enhanced than those during the 2015/16 QBO disruption suggests that the weak positive wave forcing may have induced the weak westerly jet.

Second, the contributions from the parameterized CGWs and IG waves to the negative forcing at 43 hPa (Fig. 4) are much smaller than those in the 2015/16 QBO disruption (Fig. 4). As shown in Figs. 11 and 12, the source-level westward CGW momentum flux and IG wave flux at 70 hPa are only slightly larger than those of the climatology, possibly related to slightly stronger convective activity than the climatology (Figs. S5 in the Supplement and 9). The smaller CGW forcing is also explained by the vertical wind shear at $\sim$ 40 hPa in January 2019 (Fig. 4d) being smaller than in February 2016 (Fig. 4d of KCG20). Weaker convective activity in 2019/20 could be related to the El Niño phase, which was much weaker than in 2015/16.

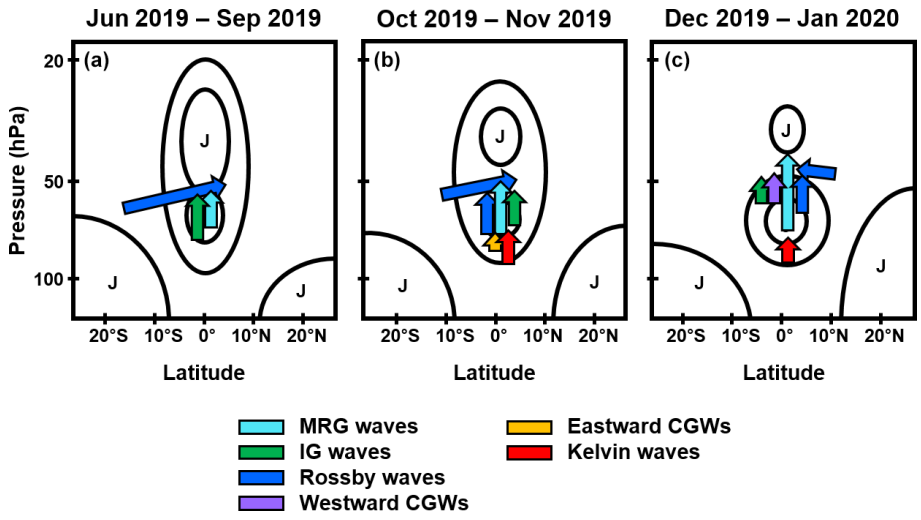

Figure 14. Schematic of the zonal-mean zonal wind (black contour) and the wave forcing anomaly compared to the climatology (arrow) during the 2019/20 QBO disruption in June 2019–September 2019 **(a)**, October 2019–November 2019 **(b)**, and December 2019–January 2020 **(c)**. "J" denotes a westerly jet.

4 Summary and conclusions

In this study, we examined the role of each equatorial planetary wave mode and parameterized convective gravity waves (CGWs) in the 2019/20 QBO disruption and compared with the results from the 2015/16 QBO disruption (KCG20). Using MERRA-2 model-level data, we separated each equatorial wave mode (Kim and Chun, 2015) and obtained small-scale CGW forcing by performing an offline CGW parameterization (Kang et al., 2017). The main results are summarized schematically in Fig. 14 and in the following text.

- From June to September 2019, unusually strong Rossby wave forcing at $\sim$ 50 hPa decelerated the westerly QBO jet at 0–5° N. The strong Rossby wave flux propagated mostly from the SH midlatitudes due to the large wave activity associated with the 2019 minor SSW in the SH and the westerly anomalies in the SH subtropics. MRG and IG wave forcing partly contributed to the wind deceleration.

- From October to November 2019, laterally propagating Rossby wave flux from the SH was weakened, with the vertically propagating Rossby wave flux from the tropics being enhanced. MRG wave forcing increased with nearly the same contribution as that from the latitudinally propagating Rossby waves. Furthermore, the IG wave forcing began to increase, albeit with a smaller magnitude than that of the MRG wave forcing. In this period, the oval-shaped structure of the QBO westerlies seen in the latitude–altitude cross section was significantly deformed.

- From December 2019 to January 2020, the momentum forcing by the MRG waves was stronger than that by any other equatorial waves, mainly due to the strong barotropic instability at the QBO edges at 70–90 hPa and partly due to the enhanced convective activity, as in the 2015/16 QBO disruption. Rossby waves propagating from the NH midlatitudes also decelerated the QBO jet. In January, the QBO westerly changed to easterly at 43 hPa. The CGWs strengthen the negative wind shear near the Equator by exerting negative forcing at 40–50 hPa by 11 % of the total negative wave forcing. The negative CGWD in this period did not show a significant increase due to a less evident increase in the convective activity and eastward shift of the convection moving speed compared to the climatology. In this period, the magnitude of the westward IG wave momentum flux was slightly larger than that of the climatology at 70 hPa owing to slightly stronger convection and the narrower critical-level filtering range.

- From November 2019 to January 2020, the Kelvin waves, and partly the CGWs, exert positive forcing on the westerly QBO wind at 60–80 hPa. This finding is important, as it implies that the zonal wind at 60–80 hPa could have been decelerated by negative wave forcing in the absence of positive momentum forcing.

It is interesting that the midlatitude Rossby waves intruded into the tropics when the tropical vertical upwelling was exceptionally strong (February 2016; August–September 2019). This relationship appears to be intuitive because a strong midlatitude Rossby wave forcing in the stratosphere drives a strong BDC. The instantaneous upward extension of the WQBO due to the strong BDC likely facilitated the QBO disruption by preventing the negative wave forcing from decelerating the top and bottom of the QBO. Therefore, the

tropical branch of the BDC and its possible influence on the 2015/16 and 2019/20 QBO disruptions should be further examined.

The 2019/20 QBO disruption occurred under the following conditions: (i) strong horizontal component of the Rossby wave forcing that originated from the SH in the early stages, (ii) strong MRG wave forcing generated from the barotropic instability at the QBO edges in the later stages, and (iii) negative IG and CGW forcing due to the slightly enhanced convective activity and westerly anomalies in the upper troposphere–lower stratosphere (UTLS). Therefore, the westerly anomalies in the subtropics and tropics as well as the strong baroclinic instability in the lower stratosphere mainly led to anomalously strong wave forcing, which in turn led to the QBO disruption. The findings of this study and KCG20 indicate considerable differences in the temporal evolutions of the wave forcing driving the 2015/16 and 2019/20 QBO disruptions (see Sect. 3.7). However, both disruptions involved significant contributions from midlatitude Rossby waves under environmental conditions that are favorable for equatorward propagation and the MRG waves that are generated in situ from the barotropic instability. In this regard, a better understanding of the two wave modes can help enhance the predictability of the QBO disruption and the associated atmospheric phenomena in the troposphere (e.g., Madden–Julian oscillation). A more frequent occurrence of QBO disruptions in the future has been suggested by previous studies, mainly due to the increase in the Rossby wave flux propagating toward the Equator and weakening of the QBO amplitude with climate changes. Moreover, considering the large contribution of equatorial planetary and gravity waves to the two QBO disruption cases, it is also necessary to investigate how these waves will change with climate change and how this change will affect the more frequent occurrence of QBO disruptions.

Data availability. The MERRA-2 data are available from the Global Modeling and Assimilation Office at NASA Goddard Space Flight Center through the NASA GES DISC online archive (available online at https://doi.org/10.5067/WWQSXQ8IVFW8, GMAO, 2015).

Supplement. The supplement related to this article is available online at: https://doi.org/10.5194/acp-21-9839-2021-supplement.

Author contributions. HYC and MJK conceived the study, and MJK perform it. MJK drafted the paper with a contribution from HYC.

Competing interests. The authors declare they have no conflict of interest.

Disclaimer. Publisher's note: Copernicus Publications remains neutral with regard to jurisdictional claims in published maps and institutional affiliations.

Acknowledgements. This work was supported by a National Research Foundation of Korea (NRF) grant funded by the Korean government (MSIT) (no. 2020R1A4A1016537). The authors thank the editor and two anonymous reviewers for their constructive comments.

Financial support. This research has been supported by the National Research Foundation of Korea (grant no. 2020R1A4A1016537).

Review statement. This paper was edited by Peter Haynes and reviewed by two anonymous referees.

References

Andrews, D. G., Holton, J. R., and Leovy, C. B.: Middle Atmosphere Dynamics, Academic, San Diego, California, 1987.

Anstey, J. A., T. P. Banyard, N. Butchart, L. Coy, P. A. Newman, S. Osprey, and C. Wright: Quasi-biennial oscillation disrupted by abnormal Southern Hemisphere stratosphere, Earth and Space Science Open Archive, https://doi.org/10.1002/essoar.10503358.1, (las access: 26 June 2020), 2020.

Barton, C. A. and McCormack, J. P.: Origin of the 2016 QBO disruption and its relationship to extreme El Niño events, Geophys. Res. Lett., 44, 11150–11157, https://doi.org/10.1002/2017GL075576, 2017.

Choi, H.-J. and H.-Y. Chun: Momentum flux spectrum of convective gravity waves. Part I: An update of a parameterization using mesoscale simulations, J. Atmos. Sci., 68, 739–759, https://doi.org/10.1175/2010JAS3552.1, 2011.

Collins, M., An, S.-I., Cai, W., Ganachaud, A., Guilyardi, E., Jin, F.-F., Jochum, M., Lengaigne, M., Power, S., Timmermann, A., Vecchi, G., and Wittenberg, A.: The impact of global warming on the tropical Pacific Ocean and El Niño, Nat. Geosci., 3, 391–297, https://doi.org/10.1038/ngeo868, 2010.

Coy, L., Newman, P. A., Pawson, S., and Lait, L. R.: Dynamics of the disrupted 2015/16 quasi-biennial oscillation, J. Climate, 30, 5661–5674, https://doi.org/10.1175/JCLI-D-16-0663.1, 2017.

Dakos, V., Carpenter, S. R., Brock, W. A., Ellison, A. M., Guttal, V., Ives, A. R., Kéfi, S., Livina, V., Seekell, D. A., van Nes, E. H., and Scheffer, M: Methods for detecting early warnings of critical transitions in time series illustrated using simulated ecological data, PloS one, 7, e41010, https://doi.org/10.1371/journal.pone.0041010, 2012.

Ebdon, R. A.: Notes on the wind flow at 50 mb in tropical and subtropical regions in January 1957 and in 1958, Q. J. Roy. Meteor. Soc., 86, 540–542, 1960.

Eswaraiah, S., J.-H. Kim, W. Lee, J. Hwang, K. N. Kumar, and Y. H. Kim: Unusual changes in the Antarctic middle atmosphere during the 2019 warming in the South-

ern Hemisphere, Geophys. Res. Lett., 47, e2020GL089199, https://doi.org/10.1029/2020GL089199, 2020.

Garcia, R. R. and Richter, J. H.: On the momentum budget of the quasi-biennial oscillation in the Whole Atmosphere Community Climate Model, J. Atmos. Sci., 76, 69–87, https://doi.org/10.1175/JAS-D-18-0088.1, 2019.

Gelaro, R., McCarty, W., Suarez, M. J., Todling, R., Molod, A., Takacs, L., Randles, C. A., Darmenov, A., Bosilovich, M. G., Reichle, R., Wargan, K., Coy, L., Cullather, R., Draper, C., Akella, S., Buchard, V., Conaty, A., da Silva, A. M., Gu, W., Kim, G.-K., Koster, R., Lucchesi, R., Merkova, D., Nielsen, J. E., Partyka, G., Pawson, S., Putman, W., Rienecker, M., Schubert, S. D., Sienkiewicz, M., and Zhao, B.: The Modern-Era Retrospective Analysis for Research and Applications, Version 2 (MERRA-2), J. Climate, 30, 5419–5454, https://doi.org/10.1175/JCLI-D-16-0758.1, 2017.

GISTEMP Team: GISS Surface Temperature Analysis (GISTEMP), version 4. NASA Goddard Institute for Space Studies, dataset, https://data.giss.nasa.gov/gistemp/ (last access: 10 September 2020), 2020.

GMAO: MERRA-2 inst3_3d_asm_Nv: 3D, 3-hourly, instantaneous, model-level, assimilation, assimilated meteorological fields, version 5.12.4. Greenbelt, MD, USA, Goddard Earth Sciences Data and Information Services Center (GES DISC), https://doi.org/10.5067/WWQSXQ8IVFW8 (last access: 1 July 2020), 2015.

Hirota, N., Shiogama, H., Akiyoshi, H., Ogura, T., Takahashi, M., Kawatani, Y., Kimoto, M., and Mori, M.: The influences of El Niño and Arctic sea-ice on the QBO disruption in February 2016, npj Climate and Atmospheric Science, 1, 10, https://doi.org/10.1038/s41612-018-0020-1, 2018.

Jewtoukoff, V., Plougonven, R., and Hertzog, A.: Gravity waves generated by deep tropical convection: Estimates from balloon observations and mesoscale simulations, J. Geophys. Res.-Atmos., 118, 9690–9707, https://doi.org/10.1002/jgrd.50781, 2013.

Kang, M.-J., Chun, H.-Y., and Kim, Y.-H.: Momentum flux of convective gravity waves derived from an offline gravity wave parameterization. Part I: Spatiotemporal variations at source level, J. Atmos. Sci., 74, 3167–3189, https://doi.org/10.1175/JAS-D-17-0053.1, 2017.

Kang, M.-J., Chun, H.-Y., and Garcia, R. R.: Role of equatorial waves and convective gravity waves in the 2015/16 quasi-biennial oscillation disruption, Atmos. Chem. Phys., 20, 14669–14693, https://doi.org/10.5194/acp-20-14669-2020, 2020.

Kim, Y.-H. and Chun, H.-Y.: Contributions of equatorial wave modes and parameterized gravity waves to the tropical QBO in HadGEM2, J. Geophys. Res.-Atmos., 120, 1065–1090, https://doi.org/10.1002/2014JD022174, 2015.

Kumar, K. K., Mathew, S. S., and Subrahmanyam, K. V.: Anomalous tropical planetary wave activity during 2015/2016 quasi biennial oscillation disruption, J. Atmos. Sol.-Terr. Phy., 167, 184–189, https://doi.org/10.1016/j.jastp.2017.12.004, 2018.

Li, H., Pilch Kedzierski, R., and Matthes, K.: On the forcings of the unusual Quasi-Biennial Oscillation structure in February 2016, Atmos. Chem. Phys., 20, 6541–6561, https://doi.org/10.5194/acp-20-6541-2020, 2020.

Lin, P., Held, I., and Ming, Y.: The early development of the 2015/16 quasi-biennial oscillation disruption, J. Atmos. Sci., 76, 821–836, https://doi.org/10.1175/JAS-D-18-0292.1, 2019.

Lindzen, R. S.: Turbulence and stress owing to gravity wave and tidal breakdown, J. Geophys. Res., 86, 9707–9714, https://doi.org/10.1029/JC086iC10p09707, 1981.

Naujokat, B.: An update of the observed quasi-biennial oscillation of the stratospheric winds over the tropics, J. Atmos. Sci., 43, 1873–1877, https://doi.org/10.1175/1520-0469(1986)043<1873:AUOTOQ>2.0.CO;2, 1986.

Osprey, S. M., Butchart, N., Knight, J. R., Scaife, A. A., Hamilton, K., Anstey, J. A., Schenzinger, V., and Zhang, C.: An unexpected disruption of the atmospheric quasi-biennial oscillation, Science, 353, 1424–1427, https://doi.org/10.1126/science.aah4156, 2016.

Raphaldini, B., Wakate Teruya, A. S., Silva Dias, P. L., Chavez Mayta, V. R., and Takara, V. J.: Normal mode perspective on the 2016 QBO disruption: Evidence for a basic state regime transition, Geophys. Res. Lett., 47, e2020GL087274, https://doi.org/10.1029/2020GL087274, 2020.

Reed, R. J., Campbell, W. J., Rasmussen, L. A., and Rogers, R. G.: Evidence of a downward propagating annual wind reversal in the equatorial stratosphere, J. Geophys. Res., 66, 813–818, 1961.

Shen, X., Wang, L., and Osprey, S.: Tropospheric forcing of the 2019 Antarctic sudden stratospheric warming, Geophys. Res. Lett., 47, e2020GL089343, https://doi.org/10.1029/2020GL089343, 2020.

Song, I.-S. and Chun, H.-Y.: Momentum flux spectrum of convectively forced internal gravity waves and its application to gravity wave drag parameterization. Part I: Theory, J. Atmos. Sci., 62, 107–124, https://doi.org/10.1175/JAS-3363.1, 2005.

Tweedy, O. V., Kramarova, N. A., Strahan, S. E., Newman, P. A., Coy, L., Randel, W. J., Park, M., Waugh, D. W., and Frith, S. M.: Response of trace gases to the disrupted 2015–2016 quasi-biennial oscillation, Atmos. Chem. Phys., 17, 6813–6823, https://doi.org/10.5194/acp-17-6813-2017, 2017.

Wheeler, M. and Kiladis, G. N.: Convectively coupled equatorial waves: Analysis of clouds and temperature in the wavenumber–frequency domain, J. Atmos. Sci., 56, 374–399, 1999.